

# The Heavy Photon Search Test Detector

C. Field<sup>a</sup>, P. Hansson Adrian<sup>a</sup>, N. Graf<sup>a</sup>, M. Graham<sup>a</sup>, G. Haller<sup>a</sup>, R. Herbst<sup>a</sup>, J. Jaros<sup>a</sup>, T. Maruyama<sup>a</sup>, J. McCormick<sup>a</sup>, K. Moffeit<sup>a</sup>, T. Nelson<sup>a</sup>, H. Neal<sup>a</sup>, A. Odian<sup>a</sup>, M. Oriunno<sup>a</sup>, S. Uemura<sup>a</sup>, D. Walz<sup>a</sup>, A. Grillo<sup>b</sup>, V. Fadeyev<sup>b</sup>, O. Moreno<sup>b</sup>, W. Cooper<sup>c</sup>, S. Boyarinov<sup>d</sup>, V. Burkert<sup>d</sup>, A. Deur<sup>d</sup>, H. Egiyan<sup>d</sup>, L. Elouadrhiri<sup>d</sup>, A. Freyberger<sup>d</sup>, F.-X. Girod<sup>d</sup>, V. Kubarovskiy<sup>d</sup>, Y. Sharabian<sup>d</sup>, S. Stepanyan<sup>d</sup>, M. Ungaro<sup>d</sup>, B. Wojtsekhowski<sup>d</sup>, R. Essig<sup>e</sup>, M. Holtrop<sup>f</sup>, K. Slifer<sup>f</sup>, S. K. Phillips<sup>f</sup>, A. Fradi<sup>g</sup>, B. Guegan<sup>g</sup>, M. Guidal<sup>g</sup>, S. Niccolai<sup>g</sup>, S. Pisano<sup>g</sup>, E. Rauly<sup>g</sup>, P. Rosier and D. Sokhan<sup>g</sup>, P. Schuster<sup>h</sup>, N. Toro<sup>h</sup>, N. Dashyan<sup>i</sup>, N. Gevorgyan<sup>i</sup>, R. Paremuzyan<sup>i</sup>, H. Voskanyan<sup>i</sup>, M. Khandaker<sup>j</sup>, C. Salgado<sup>j</sup>, M. Battaglieri<sup>k</sup>, R. De Vita<sup>k</sup>, S. Bueltmann<sup>l</sup>, L. Weinstein<sup>l</sup>, G. Ron<sup>m</sup>, P. Stoler<sup>n</sup>, A. Kubarovskiy<sup>n</sup>, K. Griffioen<sup>o</sup>

<sup>a</sup>SLAC National Accelerator Laboratory, Menlo Park, CA 94025

<sup>b</sup>University of California, Santa Cruz, CA 95064

<sup>c</sup>Fermi National Accelerator Laboratory, Batavia, IL 60510-5011

<sup>d</sup>Thomas Jefferson National Accelerator Facility, Newport News, Virginia 23606

<sup>e</sup>Stony Brook University, Stony Brook, NY 11794-3800

<sup>f</sup>University of New Hampshire, Department of Physics, Durham, NH 03824

<sup>g</sup>Institut de Physique Nucléaire d'Orsay, IN2P3, BP 1, 91406 Orsay, France

<sup>h</sup>Perimeter Institute, Ontario, Canada N2L 2Y5

<sup>i</sup>Yerevan Physics Institute, 375036 Yerevan, Armenia

<sup>j</sup>Norfolk State University, Norfolk, Virginia 23504

<sup>k</sup>Istituto Nazionale di Fisica Nucleare, Sezione di Genova e Dipartimento di Fisica dell'Università, 16146 Genova, Italy

<sup>l</sup>Old Dominion University, Norfolk, Virginia 23529

<sup>m</sup>Hebrew University of Jerusalem, Jerusalem, Israel

<sup>n</sup>Rensselaer Polytechnic Institute, Department of Physics, Troy, NY 12181

<sup>o</sup>The College of William and Mary, Department of Physics, Williamsburg, VA 23185

---

## Abstract

Heavy photons, aka "hidden sector" or "dark" photons, are massive cousins to the SM photon, which couple to an analogue of electric charge. They arise naturally in theories with additional U(1) gauge groups, and have been proposed as a possible explanation for the muon g-2 anomaly, astrophysical puzzles, and possible sightings of light dark matter in direct detection experiments. Masses in the range 10 to 1000 MeV are suggested. Heavy photons couple weakly to electric charge, so can be produced via electroproduction and can decay into electron-positron pairs, albeit at rates strongly suppressed compared to standard QED trident processes. Consequently, heavy photons must be identified above copious backgrounds, requiring high luminosity/high rate experiments, good mass resolution (to identify invariant mass bumps), and good vertexing (to see the long lifetimes implied by weak couplings). The Heavy Photon Search (HPS) will use a silicon microstrip vertex tracker triggered by a high speed PbWO<sub>4</sub> electromagnetic calorimeter to search for these states in a fixed target experiment at Thomas Jefferson National Accelerator Facility (JLab). The first stage of HPS was the HPS Test Run experiment, designed to demonstrate the technical feasibility of the detector and data acquisition systems and to confirm that critical backgrounds were correctly modeled. This paper describes the HPS Test Run detector, reviews its performance, and presents results of the normalized trigger rate measurements that confirm the accuracy of the background simulation.

**Keywords:** silicon microstrips, tracking, vertexing, heavy photon, electromagnetic calorimeter

---

\*Corresponding author

Email address: phansson@slac.stanford.edu (P. Hansson Adrian)

## Contents

<b>1</b>	<b>Introduction</b>	<b>3</b>
<b>2</b>	<b>Detector Overview</b>	<b>4</b>
<b>3</b>	<b>The HPS Test Beamline</b>	<b>5</b>
<b>4</b>	<b>Silicon Vertex Tracker</b>	<b>5</b>
4.1	Layout . . . . .	6
4.2	Components . . . . .	7
4.3	Digitization, Event Building and Data Transmission . . . . .	8
4.4	Production, Assembly and Shipping . .	8
4.5	Alignment . . . . .	9
<b>5</b>	<b>Electromagnetic Calorimeter</b>	<b>9</b>
5.1	Components . . . . .	9
5.2	Layout . . . . .	9
5.3	Signal readout . . . . .	10
<b>6</b>	<b>Trigger and Data Acquisition</b>	<b>10</b>
6.1	Trigger system . . . . .	10
6.2	Data Acquisition and Online Computing	12
<b>7</b>	<b>Performance</b>	<b>12</b>
7.1	SVT Performance . . . . .	12
7.1.1	Cluster and Hit Reconstruction .	12
7.1.2	Momentum and Vertexing Resolution . . . . .	14
7.2	ECal Performance . . . . .	14
7.3	Trigger Performance . . . . .	15
<b>8</b>	<b>Multiple Coulomb Scattering Distributions</b>	<b>16</b>
8.1	Multiple Coulomb Scattering Models .	16
8.2	Running Conditions . . . . .	16
8.3	Measured Angular Distributions . . . .	17
8.4	Conclusion . . . . .	18
<b>9</b>	<b>Summary and Outlook</b>	<b>18</b>
<b>10</b>	<b>Acknowledgements</b>	<b>18</b>

## 1. Introduction

One of the more striking anomalies in recent astrophysical observations is an excess of high energy electrons and positrons consistent with a large, unknown source of pair production [1, 2]. The existence of a massive, hidden sector vector boson; a “dark photon,” that mixes kinetically with the Standard Model photon and mediates annihilation or decay of dark matter particles is a theoretically attractive explanation of this cosmic-ray excess [3][4].

Heavy photons, aka “hidden sector” or “dark” photons, are particles with mass 10-1000 MeV which couple weakly to the SM photon, so can be radiated by electrons, and can decay into  $e^+e^-$  pairs, albeit at rates far below those of QED trident processes. They have been suggested by numerous Beyond Standard Model theories and as an explanation of the current muonic  $g-2$  anomaly, and may couple directly to hidden sector particles that may constitute all or some of the dark matter. Current phenomenology highlights the 20-1000 MeV/c<sup>2</sup> mass range, and suggests that heavy photons couple to electric charge with strength  $\epsilon e$ , where  $\epsilon$  is in the range of  $10^{-3} - 10^{-5}$ . This range of parameters makes heavy photon searches viable at electron-positron colliders and in moderate energy fixed target electroproduction, and results from both approaches have already been reported. Fixed target experiments offer the highest sensitivity for heavy photons with mass  $< 1000$  MeV/c<sup>2</sup> [5], but require large data sets and good mass resolution to identify a small mass peak above the copious QED background. At small couplings, heavy photons become long-lived, so detection of a secondary decay vertex can reject the prompt QED background and boost experimental sensitivity. The HPS experiment uses both invariant mass and vertex signatures by placing a  $\approx 1$  m long silicon tracking and vertexing detector (10 cm) downstream of a 0.25 %X<sub>0</sub> tungsten) target and inside a dipole magnet [6]. The experiment runs at high rates, exploiting the 100% duty cycle of the CEBAF accelerator to accumulate the need statistics. The trigger is provided by a fast electromagnetic calorimeter just downstream of the magnet.

The HPS Test run, a simplified version of the full HPS experiment, was proposed and approved at JLab as the first stage of the HPS experiment. Its purposes included demonstrating that the apparatus and data acquisition systems are technically feasible and that the trigger rates and occupancies encountered in electron-beam running are as simulated. Given dedicated running time with

electron beams, the HPS Test Run apparatus is capable of searching for heavy photons in unexplored regions of parameter space. The HPS Test apparatus was installed on April 19, 2012, and ran parasitically with the HDice experiment, using its photon beam, until May 18. The JLab run schedule precluded any dedicated electron beam running, but the HPS Test Run was allowed a short and valuable dedicated run with the photon beam.

This paper reviews the HPS Test Run apparatus; documents the successful performance of the trigger, data acquisition, silicon tracker, and ECal at the level assumed in calculating the physics reach of the experiment. Of particular importance, data from the dedicated photon beam running has been used to compare the measured trigger rates with those expected in simulation. The Test Run trigger rate is almost entirely due to photons which have converted to  $e^+e^-$  pairs in a thin target upstream of HPS and it is sensitive to their multiple Coulomb scattering in the conversion target. During electron beam running, the tails of the multiply Coulomb scattered primary beam are the dominant source of occupancy in the tracker and trigger rate in the electromagnetic calorimeter. The trigger rates in the Test Run are also sensitive to the tails of the multiple Coulomb scattering distribution. Good agreement between the measured and simulated rates confirms our understanding of multiple Coulomb scattering and the reliability of the background simulation used to benchmark the physics reach of the HPS experiment.

Searching for a small signal on a large background requires high statistics. This in turn requires the experiment operate with high beam currents, handle very high data rates, and tolerate high radiation levels. In particular, the following are required:

- large and uniform acceptance in the forward region close to the beam in order to catch boosted heavy photon decay products,
- beam passage through the apparatus in vacuum, to eliminate direct interactions with the detector and minimize beam gas interactions,
- a flexible, redundant and efficient trigger selecting electron and positron pairs at rates up to 50kHz,
- excellent track reconstruction efficiency for electrons and positrons,
- good angular and momentum resolution to reconstruct invariant mass precisely,
- excellent vertex resolution to discriminate displaced heavy photon decays from prompt QED backgrounds,

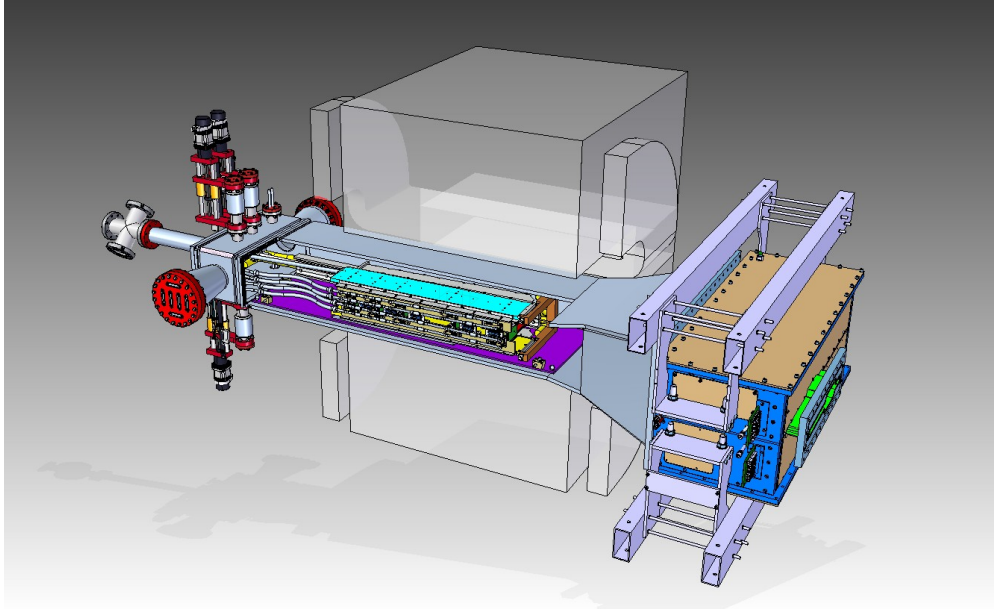


Figure 1: Rendering of the HPS Test apparatus installed on the beam line.

- high rate electronics with excellent timing resolution to minimize out of time backgrounds,
- data handling rates of 100 MB/s to permanent storage,
- detector components that can survive and efficiently operate in a high radiation environment with local doses exceeding 100 Mrad.

## 2. Detector Overview

The HPS experiment will run in Hall B at JLab using the CEBAF electron beam, a 499 MHz beam at energies ranging up to 11 GeV and currents up to 800 nA. The design of the experiment follows from the kinematics of A' production which typically results in final state particles within a few degrees of the incoming beam, especially at low  $m_{A'}$ . So detectors must be placed close to the beam. The intense electron beam and the degraded electrons produced in the target and spread out horizontally by the analyzing magnet constitute a "dead zone" which must be completely avoided, so the apparatus is split vertically above and below the beam plane. The beam is transported in vacuum to minimize beam gas backgrounds. Even so, background rates in the detectors remain high, so high rate detectors, a fast trigger, and excellent time tagging are required to minimize their impact. At masses below  $2m_\mu$  only decays to

electrons are allowed, so the key trigger comes from a lead-tungstate calorimeter with 250 MHz readout.

A rendering of the HPS Test apparatus installed on the beam line is shown in Fig. 1. Most technologies used in the HPS Test apparatus will be used in the HPS detector with some improvements to each of the systems; both from lessons learned during running of the HPS Test but also from less schedule and budget constraints.

An overview of the coverage, segmentation and performance of the HPS Test detector is given in Tab. 1.

The silicon tracking and vertexing detector for HPS Test, or SVT, operates in an existing vacuum chamber inside the pair spectrometer analyzing magnet in Hall B at JLab. The design principles of the SVT are described in further detail in the HPS Test Run Proposal [7]. There are five measurement stations, or "layers," placed immediately downstream of the target. Each layer comprises a pair of closely-spaced planes and each plane is responsible for measuring a single coordinate, or "view." Introduction of a stereo angle between the two planes of each layer provides three-dimensional tracking and vertexing throughout the acceptance of the detector with one redundant layer.

In order to accommodate the dead zone, the SVT is built in two halves that are mirror reflections of one another about the plane of the nominal electron

Table 1: Overview of the coverage, segmentation and performance of the HPS Test detector.

System	Coverage (mrad)	# channels	ADC (bit)	Time resolution (ns)	# layers	Segmentation	Performance
SVT	$15 < \theta_y < XXXX$	12800	14	$\approx 2$ ns	5 (stereo layers)	$\approx 120 \mu\text{m} r - \phi$ $\approx 6 \mu\text{m} z$	$\sigma_{d0,y} \approx 100 \mu\text{m}$ $\sigma_{d0,x} \approx 300 \mu\text{m}$ $\sigma_{d0,z} \approx 1 \text{ mm}$
Ecal	$15 < \theta_y < XXXX$	442	12	4 ns	1	$1.3 \times 1.3 \text{ cm}^2$ $1.6 \times 1.6 \text{ cm}^2$	$\sigma(E)/E \approx 4.5\%$

beam. Each half consists of five double-sided modules mounted on a support plate that provides services to the modules and allows them to be moved as a group relative to the dead zone. Each module places a pair of silicon microstrip sensors back-to-back at a specified stereo angle with independent cooling and support.

Each half of the electromagnetic calorimeter, or ECal, consists of 221 PbWO<sub>4</sub> crystals arranged in rectangular formation. There are five rows with 46 modules in each row except the row closest to the beam plane which has 37. The light from each crystal is read out by Avalanche Photodiode (APD) glued on the back surface of the crystal. Signals from the APDs were amplified using custom-made amplifier boards before being sent to the readout electronics.

The Data Acquisition system combines two architectures, the Advanced Telecom Communications Architecture (ATCA) based SVT readout system and VXS based digitization and triggering system for the ECal. The system was designed to run at up to a 20 kHz trigger rate.

### 3. The HPS Test Beamline

The HPS Test run studied multiple Coulomb scattering of electrons and positrons from bremsstrahlung photons produced in the Hall-B tagged photon facility. Figure 2 shows the layout of the HPS Test setup on the beam line. The SVT was installed inside the Hall B pair spectrometer magnet (PS) vacuum chamber with the ECal mounted downstream of it. Both the SVT and the ECal were retracted off the beam plane to allow clean passage of the photon beam through the system.

The photon beam was generated in the interaction of the 5.5 GeV electrons with a gold radiator of  $10^{-4} X_0$ , located  $\approx 9$  m upstream of the PS. The primary beam and scattered electrons are deflected away from detectors by the dipole magnet of the photon tagging system. After collimation (6.4 mm diameter), the photon beam passes through the aluminum PS pair converter and later the HPS system. The converter was located

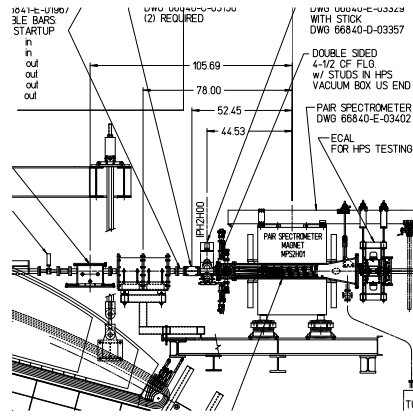


Figure 2: Layout of the HPS parasitic run.

$\approx 77$  cm upstream of the first layer of the silicon vertex tracker. Data was taken on different converters (empty,  $1.8 \times 10^{-3} X_0$ ,  $4.5 \times 10^{-3} X_0$  and  $1.6 \times 10^{-2} X_0$ ). These measurements were repeated with the reverse field setting of the PS dipole magnet.

### 4. Silicon Vertex Tracker

The Silicon Vertex Tracker (SVT) enables efficient reconstruction of charged particles and precision determination of their trajectories. These measurements allow A' decays to be distinguished from background via simultaneous estimation of the invariant mass of e<sup>+</sup>e<sup>-</sup> decay products and the position of decay vertexes downstream of the target.

The design of the SVT presents a number of significant challenges. First, the A' decay products have momenta in the range of 1 GeV, so multiple scattering dominates mass and vertexing errors for any possible material budget. Therefore, the construction of the SVT must place the smallest amount of material in the tracking volume. Second, the signal yield for long-lived A' will be very small, so the rejection of prompt vertexes must be exceedingly pure, on the order of  $10^{-7}$ , in order to eliminate all prompt backgrounds. This requires great

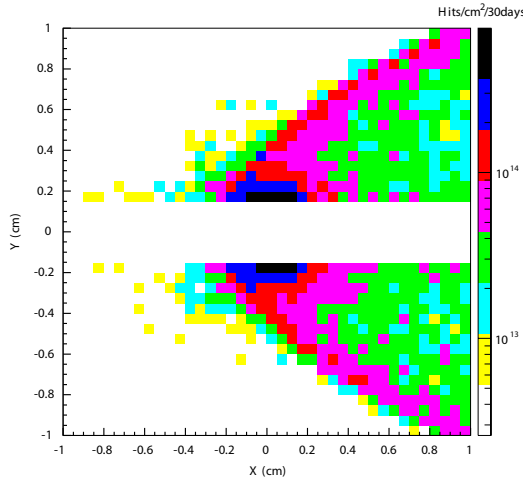


Figure 3: Simulation of the fluence 10 cm downstream of the target in the active region of the SVT ( $|Y| > 0.15$  cm) looking downstream; electrons bend towards  $+x$ .

care in design, calibration, and operation of the detector. Finally, the passage of the degraded primary beam through the apparatus creates a region of extreme occupancy and radiation that is critical for sensitivity to low-mass  $A'$  that have decay products nearly collinear with the beam. This places low-mass acceptance in opposition to tracking and vertexing purity and the longevity of the detector.

It is this last challenge that has the most interesting and obvious impacts on the design of the SVT. To achieve good vertexing performance, the first layer must be placed no more than about 10 cm downstream of the target. At that distance, it is found that the active region of a sensor can be placed as close to 1.5 mm from the center of the beam, defining a 15 mrad “dead zone” in the detector around the plane of the primary beam. At the edge of this “dead zone,” the radiation dose approaches  $10^{15}$  electrons/cm<sup>2</sup>/month, or roughly  $3 \times 10^{14}$  1 MeV neutron equivalent/cm<sup>2</sup>/month [8], as shown in Fig. 4. This requires the sensors to be actively cooled. Meanwhile, very low-energy delta rays from beam gas interactions multiply the density of background hits, so the SVT must operate inside the beam vacuum. Finally, in order to protect the sensors, the detector must be movable so that it can be retracted during periods of uncertain beam conditions.

#### 4.1. Layout

A realistic GEANT4 [9] simulation of the detector based on the SLIC simulation package [10], including all backgrounds, has been used to optimize the layout

for acceptance, tracking efficiency, mass resolution and prompt vertex rejection. The layout of the SVT is summarized in Tab. 4.1 and rendered in Fig. 4. 100 mrad stereo is used in the first three layers to provide higher-resolution 3D space points for vertexing. 50 mrad stereo in the last two layers breaks the tracking degeneracy of having five identical layers and minimizes fakes from ghost hits, improving pattern recognition while still providing sufficient pointing resolution into the third layer for robust hit association in the denser environment there. Altogether, this layout comprises 20 sensors and hybrids and 100 APV25 chips for a total of 12780 readout channels.

Layer	1	2	3	4	5
$z$ from target (cm)	10	20	30	50	70
Stereo angle (mrad)	100	100	100	50	50
Bend res. ( $\mu\text{m}$ )	$\approx 60$	$\approx 60$	$\approx 60$	$\approx 120$	$\approx 120$
Non-bend res. ( $\mu\text{m}$ )	$\approx 6$	$\approx 6$	$\approx 6$	$\approx 6$	$\approx 6$
# of sensors	4	4	4	4	4
Dead zone (mm)	$\pm 1.5$	$\pm 3.0$	$\pm 4.5$	$\pm 7.5$	$\pm 10.5$
Power cons. (W)	6.9	6.9	6.9	6.9	6.9

Table 2: Layout of the HPS Test SVT.

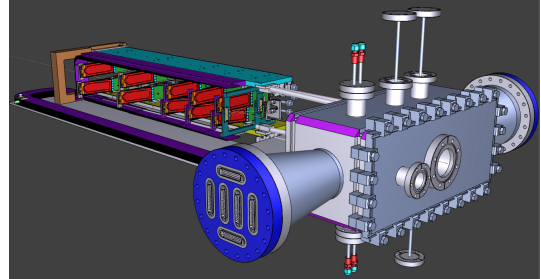


Figure 4: A rendering of the HPS Test SVT showing the modules on their support plates held by the hinged C-support on the left and the motion levers on the right. The sensors are shown in red and the hybrid readout boards in green. The beam enters from the right through a vacuum box with flanges for services.

The SVT is built in two separate halves that are mirror reflections of one another about the plane of the nominal electron beam. Each half consists of five, double-sided modules mounted on a support plate that provides services to the modules and allows them to be moved as a group relative to the dead zone. The two halves of the tracker are connected to hinges mounted on a C-shaped support just beyond the last layer t that defines the nominal spacing between the upper and lower halves of the tracker. A shaft attached to each support plate in front of layer 1 extends upstream and connects to a linear shift

that transfers motion into the vacuum box through bellows to open and close the two halves around the dead zone. The C-support is mounted to an aluminum baseplate that defines the position of the SVT with respect to the vacuum chamber. Figure 5 shows a photograph of both completed detector halves prior to final assembly.



Figure 5: Both halves of the HPS Test SVT after final assembly at SLAC. The cooling manifolds and integrated cable runs are clearly seen.

#### 4.2. Components

The sensors for the SVT are selected according to a number of requirements. First, the sensors must be radiation tolerant to approximately  $1.5 \times 10^{14}$  1 MeV neutron equivalent/cm<sup>2</sup> for a six month run. This corresponds to about 4 MHz/mm<sup>2</sup>, so the sensor and readout technology must be capable of handling very high local occupancies. Since sensitivity is limited by multiple scattering, a material budget of less than 1%  $X_0$ /layer is imperative and far less is desirable. To achieve the required vertex resolution single-hit resolutions better than XXXX  $\mu\text{m}$  are required. Finally, the sensor technology must be mature and readily available at low cost. Silicon microstrips are the best match to these requirements, and a supply of appropriate microstrip sensors purchased from the Hamamatsu Photonics Corporation for the Run 2b upgrade of the DØ experiment [11] are readily available. These are *p*-on-*n*, single sided, AC coupled, polysilicon-biased sensors fabricated on <100> silicon and have 30 (60) micron sense (readout) pitch over their  $4 \times 10 \text{ cm}^2$  surface. Although a maximum bias of 350 V is specified, the vast majority are operable to 1000 V and therefore remain fully depleted to a dose of approximately  $1.5 \times 10^{14}$  1 MeV neutron equivalent/cm<sup>2</sup>.

Because the regions of high occupancy are small spots in two dimensions, only a short length of any one strip see a significant occupancy, and the strips in that

region act as long pixels. However, the rates are still very high and lowering the peak occupancy in the sensors to approximately 1% for tracking requires a trigger window and tagging of hit times to roughly 8 ns. The FADC readout for the ECal and muon system are capable of this (see Sec. 5.3), but achieving  $2\sigma$  efficiency for silicon hits then requires 2 ns time resolution for the hits in the SVT. This performance can be achieved with the APV25 readout ASIC developed for the CMS experiment at CERN [12]. When operated in “multi-peak mode”, the APV25 captures successive samples of the output of the shaper in sets of three at a sampling rate of approximately 40 MHz. By fitting the known *CR-RC* shaping curve to these samples, the initial time of the hit can be determined to a precision of 2 ns for S/N > 25, an achievable figure with our sensors if read out individually [13]. For the SVT, six-sample readout and the shortest possible shaping time (35 ns) will be used to best distinguish hits that overlap in time. The APV25 ASICs are hosted on simple FR4 hybrids since these hybrids and their cooling system are outside the tracking volume. Along with the sensors, these are assembled into half-modules, one for each tracking view, with a short cable pigtail to provide power and configuration to the modules and signal readout.

The sensor modules for the SVT consist of a pair of identical half-modules, sandwiched back-to-back around an aluminum cooling block at one end and a similar PEEK spacer block at the other. Figure 6 shows a single module after assembly. The cooling block pro-

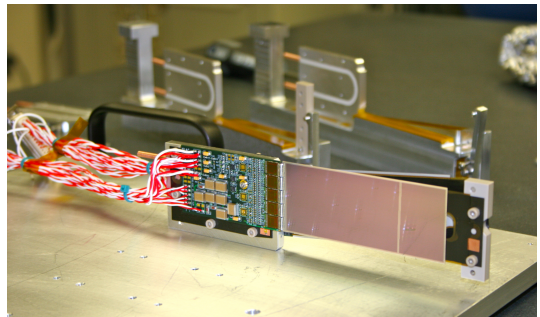


Figure 6: A prototype module assembly (foreground) with the 50 mrad (left) and 100 mrad (right) module assembly fixtures in the background. A pair of cooling blocks and a spacer block can be seen on the fixtures.

vides the primary mechanical support for the module as well as cooling via copper tubes pressed into grooves in the plates. The spacer block defines the spacing between the sensors at the far end of the module, stiffens the module structure, and improves the stability of the sensor alignments.



Figure 7: Picture of the SVT DAQ COB board with four data processing daughter cards visible.

The total power consumption of the five APV25 chips mounted on the hybrid readout board is about 2 W. Since heating from the leakage current is only significant at a single small spot on the sensor, the dominant heat load on the sensor, even after irradiation, is radiant heat from the inside wall of the vacuum chamber, less than 0.5 W per sensor. The total power consumption budget of about 40 W is removed by a water/glycol mixture circulated through a flexible manifold attached to the copper tubes in the cooling blocks. During the Test run the sensors were operated at around 23°C with a total mass flow of about XXXXg/s.

Each half module consists of a single sensor and a hybrid electronic readout board glued to a polyamide-laminated carbon fiber composite backing. A window is machined in the carbon fiber leaving only a frame around the periphery of the silicon to minimize material. A 50  $\mu\text{m}$  sheet of polyamide is laminated to the surface of the carbon fiber with 1 mm overhang at all openings to ensure good isolation between the backside of the sensor, carrying high-voltage bias, and the carbon fiber which is held near ground. The average support material in the tracking volume is approximately 0.06%  $X_0$  per double-sided module for a total material budget of 0.7% per layer.

#### 4.3. Digitization, Event Building and Data Transmission

The SVT data acquisition (DAQ) based on the Reconfigurable Cluster Element (RCE) and Cluster Interconnect (CI) concept developed at SLAC as generic building blocks for DAQ systems in high energy physics. The RCE is a generic computational building block, housed on a separate daughter card called Data Processing Module (DPM), that are realized on an ATCA front board called the Cluster On Board (COB), see Fig. 7. The Gen-I RCE used in the Test run consisted of a Virtex 5 FPGA with 1 GB of DDR3 RAM. The

outputs of 12 SVT half-modules are digitized on the Rear-Transition-Module (RTM), a custom board on the back side of the ATCA crate, interfacing the HPS readout to the generic DAQ components on the COB. A pre-amplifier converts the APV25 differential current output to a different voltage output scaled to the sensitive range of a 14-bit ADC operating at the system clock of 41.667 MHz. The RTM is organized into four sections with each section supporting three SVT half-module hybrids (15 APV25 channels). The RTM also includes a 4-channel Fiber Optic module and supporting logic which can be used to interface to the JLab trigger system supervisor. Each section of the RTM, up to three hybrids, is input to a DPM which applies thresholds for data reduction and organizes the sample data into UDP datagrams. The DPM also hosts an I2C controller used to configure and monitor the APV25 chips on those three hybrids. A single ATCA crate with two COB cards was used, one supporting four DPMs and one supporting 3 DPMs and one DPM that is configured as the trigger and data transmission module. The two COB cards and their DPMs are interconnected with a 10Gb/s switch card [14] which also hosts two 1Gb/s Ethernet interfaces to the external SVT DAQ PC.

The external PC supports three network interfaces; two standard 1Gb/s Ethernet and one custom low latency data reception card. The first Ethernet interface is used for slow control and monitoring of the 8 DPM modules. The second Ethernet interface serves as the interface to the JLAB data acquisition system. The third custom low latency network interface is used to receive data from the SVT ATCA crate and supports a low latency, reliable TTL trigger acknowledge interface to the trigger DPM. This PC hosts the SVT control and monitoring software as well as the JLab read out controller (ROC) application described in more detail in Sec. 6.2.

This system is capable of operating up to 20 kHz and XXXX MB/s which is well in line with the rates expected and observed during the HPS Test run.

#### 4.4. Production, Assembly and Shipping

Of the sensors tested during production, 90% were capable of 1000 V bias voltage without breakdown. Hybrids underwent quick QA testing and each half-module was run at low temperature ( $\approx 5^\circ \text{C}$ ) and fully characterized for pedestals, gains, noise and time response after assembly. Of 29 half-modules built, 28 passed QA testing, leaving 8 spare modules after completion of the SVT. Full-module assembly and mechanical surveys were performed at SLAC before final assembly, testing and shipping of the SVT to JLab A custom shipping container with nested crates and redundant isolation for

shock and vibration was built in order to safely send the partly assembled SVT to JLab. At JLab, the entire SVT was integrated with the full DAQ and the power supplies before moving the module-loaded support plates to Hall B for final mechanical assembly and installation inside of the vacuum chamber.

#### 4.5. Alignment

The SVT was aligned using a combination of optical, laser and touch probe surveys at SLAC and JLab. The optical survey of individual modules with precision of a few  $\mu\text{m}$  are combined with a touch-probe survey of the overall SVT support structure, with 25–100  $\mu\text{m}$  precision, to locate the silicon sensor layers with respect to the support plates and the mechanical survey balls on the base plate. After full assembly and installation of the SVT at JLab, a mechanical survey of the SVT base plate position inside the pair spectrometer vacuum chamber is used to determine the global position of the SVT with respect to CEBAF beam line. The resulting survey-based alignment has the position of the silicon sensors correct to within a few hundred microns. A more sophisticated global track-based alignment technique to reach the final alignment precision is being developed.

### 5. Electromagnetic Calorimeter

The electromagnetic calorimeter, installed downstream of the tracker, performs two essential functions for the experiment: provides a trigger to DAQ system and is used in the analysis for electron identification. The energy of electrons of interest in HPS experiment will be in the range 0.5 – 6.5 GeV. The ECal modules must have sufficient radiation lengths to absorb the full energy of these scattered electrons, have fine enough granularity to handle a high rate of electromagnetic background and survive large doses of radiation, especially near the beam plane. In addition, it needs to have excellent hit time resolution,  $< 10 \text{ ns}$ , in order to beat down beam backgrounds.

Requirements of a compact design, operation at high radiation and high rate environment, in the presence of a high magnetic field are fulfilled by a lead-tungstate ( $\text{PbWO}_4$ ) crystal calorimeter with magnetic field resistant Avalanche Photodiode (APD) readout. Such calorimeter has been operational in the inner part of the CLAS detector for experiments in Hall-B at JLab since 2005 and meet all requirements set by HPS. The modules from this calorimeter have been subsequently repurposed for the ECal.

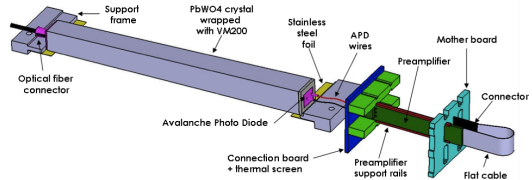


Figure 8: Schematic view of an ECal module.

#### 5.1. Components

The HPS test run ECal uses  $\text{PbWO}_4$  crystals, APDs, and preamplifier boards from the inner calorimeter (IC) of the CLAS detector[15]. In Figure 8 a schematic view of the module assembly is shown. Lead-tungstate crystals are 160 mm long and are tapered with front face of  $13.3 \times 13.3 \text{ mm}^2$ , tapered to  $16 \times 16 \text{ mm}^2$  at the rear face. The crystals were fabricated with very tight tolerances: 19  $\mu\text{m}$  for 13.3 mm dimension and 13  $\mu\text{m}$  for the 16 mm dimension. Each crystal is wrapped in VM2000 multilayer polymer mirror film. The APDs (Hamamatsu S8664-55) with  $5 \times 5 \text{ mm}^2$  active area and 75% quantum efficiency were glued on the rear face of the crystals using MeltMount 1.7 thermal plastic adhesive. The low gain of APDs ( $\sim 200$ ) was compensated with custom made preamplifier boards, which provide factor 2000 amplification of the ADP signal.

#### 5.2. Layout

Like the tracker, the electromagnetic calorimeter is split into two parts, beam-up and beam-down, to avoid impinging on the dead zone. The two parts of the Ecal are separated by a vacuum chamber, see Fig. 9. The beam and radiative secondaries pass between the two parts in vacuum, to avoid generating unnecessary backgrounds. The crystal modules in each part are arranged in rectangular formation, as shown in top panel of Fig. 9. There are 5 layers in each formation. Each layer has 46 crystals except for the layers closest to the beam plane where 9 modules were removed to allow a larger opening for the outgoing electron and photon beams. In order to have stable light yield from crystals, and stable operation of APDs and preamplifiers, the module assembly of each ECal part was enclosed inside a temperature controlled box.

Inside the box  $\text{PbWO}_4$  crystals were supported by aluminum frames stacked on top of each other. The bias voltage for APDs ( $\sim 400 \text{ V}$ ), the low voltage for preamplifiers ( $\pm 5 \text{ V}$ ), and the signals from APDs were transmitted in and out of the enclosure through a backplane called motherboard. The 221 modules in each part of



Figure 10: A Jefferson Lab FADC250 VXS module.

the ECal were divided into two low voltage groups and 12 bias voltage groups. Modules in bias voltage groups were selected to have gain uniformity of  $\sim 20\%$ .

During the test run ECal was mounted downstream of the analyzing dipole magnet at the distance of about 147 cm from the upstream edge of the magnet. The gap between innermost edge of the crystals of two parts was 7.4 cm, centered on the beam plane. The temperature stability of the system during the test run was better than  $1^\circ$  F, the temperature uniformity inside the box was better than  $4^\circ$  F.

### 5.3. Signal readout

ECal signal readout was organized as follows: the amplified APD signal from the motherboard is sent to a 2 : 1 signal splitter. After the split, 2/3 of the signal is sent a discriminator then to a Time-to-Digital Converter (TDC). The 1/3 of the signal is fed to a single channel of 16-channel JLAB Flash Amplitude-to-Digital Converter (FADC250), see Fig.10 [16]. Two 20-slot VXS crates with 14 (for top ECal) and 13 (for bottom ECal) FADC boards were employed for the test run.

The FADCs store 12-bit digitized samples at 250 MHz in  $8 \mu\text{s}$  deep pipelines. When a trigger is received, the appropriate part of the pipeline is accessed for the readout. HPS used FADCs in the integration mode. A predefined number of samples of the signal that exceeds a predefined threshold have been summed and stored in 17-bit register for readout. The number of samples for integration was defined by two parameters that could be set separately, the number of samples

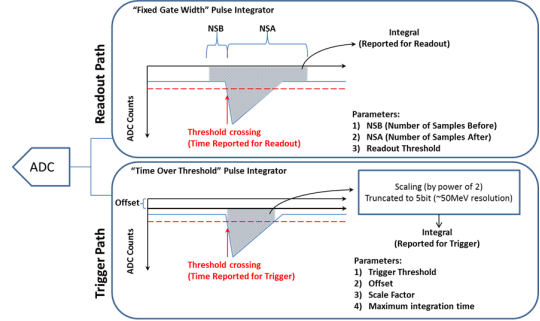


Figure 11: FADC data paths.

integrated before the signal crossed threshold (*NSB*) and the number of samples integrated after the signal crossed threshold (*NSA*), see Fig.11. This scheme significantly compresses the data input to the FADC. During data analysis, a pedestal value is subtracted to obtain the actual summed energy.

For various reasons only 385 out of 442 modules (87%) were operational during the test run. The readout threshold was set to 70 MeV, the number of samples before and after the threshold crossing were 5 and 30, respectively.

## 6. Trigger and Data Acquisition

The HPS Test apparatus DAQ handles the acquisition of data from two sub-detectors: the SVT and the ECal, with two DAQ architectures. The SVT is read-out with Advanced Telecom Communications Architecture (ATCA) hardware while the ECal uses VXS based hardware. The trigger system receives input from the ECal and distributes a trigger signal to all detector sub-systems to read out a selected event.

### 6.1. Trigger system

The HPS test run trigger system is designed to select  $e^+e^-$  events efficiently by using information from the ECal. The trigger looks for time coincidences of clusters in the top and bottom half of the ECal. The trigger system can be broken down into three sections as shown in Fig. 12:

- FADC (pulse finding): samples and digitizes the signal pulses from each detector channel. Sends the measured pulse energy and arrival time to the Crate Trigger Processor (CTP),

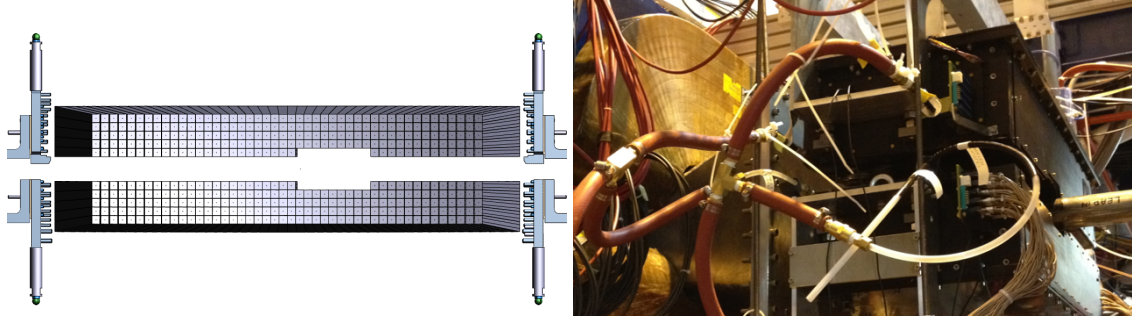


Figure 9: Layout of PbWO<sub>4</sub> modules in two halves of the ECal (left) and the ECal assembly on the beam line (right).

- CTP (cluster finding): groups FADC pulses from each half of the ECal into clusters. The cluster energy and arrival time are sent to the Sub-System Processor (SSP),
- SSP (cluster pair finding): searches for time coincidences of pairs of clusters from the top and bottom half of the ECal and applies topological selections.

The time coincidence window of pairs of clusters in the top and bottom half of the ECal are programmable with 4 ns resolution. As described above, the first stage of the trigger logic is incorporated into the FPGA's on the FADC boards. The trigger integrates using a "time-over-threshold" window as explained in Fig. 11. For triggering purposes, every channel has:

- a trigger threshold, measured in ADC counts,
- an offset,
- a conversion factor to convert ADC counts into energy in MeV, from 50 to  $\sim$  1500 MeV, with 5-bit accuracy
- an energy threshold discriminator to provide a minimum energy cutoff

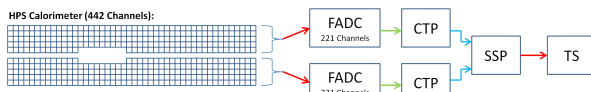


Figure 12: Block diagram of the ECAL trigger system consisting of the FADC that samples and digitizes signals for each detector channel and sends them for cluster finding in the CTP. The CTP clusters are sent to the SSP where the final trigger decision is taken based on pairs of clusters in both halves of the ECal. The decision is sent to the Trigger Supervisor (TS) that generates the necessary signals to readout the sub-detectors.

Note that the threshold for the trigger path can be set independently from the readout threshold. The offset is subtracted from ADC samples before they are integrated. The values reported to the CTP are the 5-bit pulse energy and the 3-bit time at which the pulse crossed the threshold. Data from every channel is sent to the CTP every 32 ns. With the available 3-bit time information, the CTP looks for time coincidences of crystal signals within an 8 ns window (the limit is 4 ns). The cluster finding algorithm is fast and makes use of the parallel processing capability of the FPGA's by simultaneously searching for 125 clusters, up to 3x3 in size, across the calorimeter crystal array, and it performs the following tasks:

- Adds together the energy for every 3x3 square of channels in the ECal
- Hits are added together if their leading edges occurred within a programmable number of 4 ns clock cycles (HPS test run used 8 ns coincidence time interval).
- If the 3x3 energy sum is larger than the programmable cluster energy threshold and the sum is greater than any neighboring 3x3 windows, the CTP reports the cluster parameters to the SSP.

The CTP evaluates all the hits in its half of the calorimeter every 4 ns. A programmable time window is used to allow hits that are slightly out of time with each other to be considered as part of a cluster sum. This is done by reporting hits when they occur and then reporting them again for the next  $N$  number of 4 ns clock cycles, where  $N \in [0, 7]$ . This is useful to deal with skew and jitter that develop from the detector, cabling, and electronics. As described above, the CTP only selects the 3x3 window with the highest energy sum of its neighbors. This filtering is applied to deal with overlapping clusters and cases where the cluster is larger than a 3x3 window.

The final trigger decision is made by CTPs and the SSP is passed to the Trigger Supervisor (TS). The TS generates all necessary signals and controls the entire DAQ system readout through the Trigger Interface (TI) units. The TI units are installed in every crate that participate in the readout process.

The trigger system is free-running and driven by the 250 MHz global clock and has essentially zero dead time at the occupancies expected for HPS. The Trigger Supervisor can apply dead time if necessary, for example on a ‘busy’ or ‘full’ condition from the front-end electronics. The system is designed to handle trigger rates above 50 kHz and has a latency set to  $\approx 3 \mu\text{s}$  to match that required by the SVT APV25 chip.

During the test run, for the most part the trigger system required only a single cluster in either the top or bottom Ecal module. It was tested to work up to 20 kHz trigger rates.

## 6.2. Data Acquisition and Online Computing

For the ECal, every VXS crate contains a Readout Controller (ROC) that collects digitized information, processes it, and sends it on to the Event Builder (EB). The ROC is a single blade Intel-based CPU module running DAQ software under CentOS Linux OS. For the SVT ATCA system, the ROC application runs on an embedded processor situated on the ATCA main board. The EB assembles information from the SVT and ECal ROCs into a single event which is passed to the Event Recorder (ER) that writes it to a RAID5-based data storage system capable of handling up to 100 MB/s. The EB and other critical components run on multicore Intel-based multi-CPU servers. The DAQ network system is a network router providing high-speed connections between the DAQ components and the JLab computing facility. The SVT ROC, which must handle large data volumes, has a 10 Gbit/s link to the network router, while a 1 Gbit/s link is adequate for the ECal. A 10 Gbit/s up-link to the JLab computing facility is used for long-term storage.

The SVT DAQ is described in more detail in Sec. 4.3.

## 7. Performance

### 7.1. SVT Performance

During the duration of the test run all SVT modules and APV25 chips were configured to their nominal operating points [17] with all sensors reverse-biased at 180 V. The sensors were operated within a temperature range of 20 – 24°C throughout the test run. Throughout the duration of the test run, approximately 97% of the

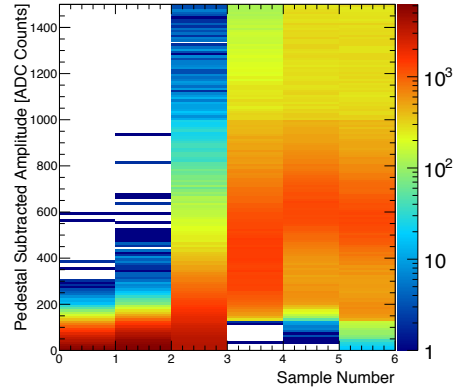


Figure 13: The six pedestal subtracted samples from individual channels associated with a hit on a track.

12,780 SVT channels were found to be operating normally. The fraction of dead or noisy channels varied from 2.4% to 4.7%. Most of these were due to misconfigured readout chips (2–4 misconfigured chips out of 100), a known noisy half-module and a couple of known noisy readout chips.

#### 7.1.1. Cluster and Hit Reconstruction

After a trigger is received, six samples of the corresponding output of the APV25 shaper circuit are digitized. The samples from every channel on a sensor surviving the data reduction algorithm (see Sec. 4.3) are the basis for offline hit reconstruction. The six samples of the APV25 shaper output are fitted to an ideal  $CR - RC$  function to extract the amplitude and the  $t_0$  of the hit. The typical pulse shape obtained is shown in Fig. 13 also demonstrates that the SVT was well timed in to the trigger with the rise of the pulse at the 3rd sampling point.

These hits are passed through a simple clustering algorithm which forms clusters by grouping adjacent strips. The position of a cluster on the sensor is determined by the amplitude-weighted mean. With a linear gain up to  $\approx 3$  MIPs, the cluster charge for hits associated with a track follow the characteristic Landau shape as expected, see Fig. 14. A noise level between  $1.1 - 1.5 \times 10^3$  electrons was established through multiple calibration runs giving a signal to noise ratio of 21 – 25. Lab-based radioactive source tests was used to provide the absolute charge normalization.

After clustering hits on a sensor, the hit time for each cluster is computed as the amplitude-weighted average of the fitted  $t_0$  channel times. The  $t_0$ -resolution is stud-

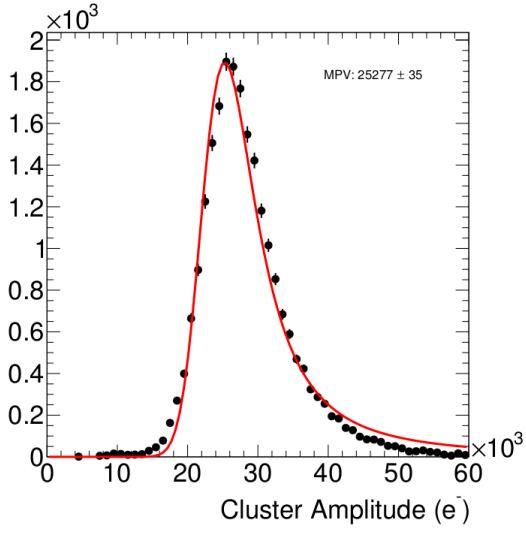


Figure 14: The cluster charge distribution for hits associated with a track.

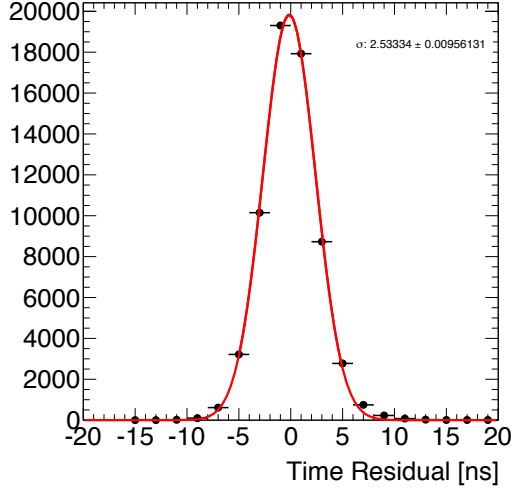


Figure 15: The cluster time residual for a representative sensor relative to the track time (see text for more details).

ied by comparing the cluster hit time with the average of all cluster hit times on the track, the “track time”, which has the expected jitter due to clock phase and trigger, approximately 25 ns. Figure 15 shows the residual to the individual cluster times. After correcting for offsets from each sensor (time-of-flight, clock phase) and accounting for the correlation between the  $t_0$  and track time, the extracted  $t_0$  resolution is 2.6 ns. This is somewhat worse than the approximately 2 ns resolution expected which we attribute to the true pulse shape differing from our idealized fit function which will be improved in the future. Reducing the APV25 pulse shaping time will also improve time resolution. These results show that we can operate with the six sample readout mode of the APV25 chip and achieve time resolution adequate for pileup rejection during electron running in the HPS experiment.

While occupancy was slightly larger than expected, good agreement between data and simulation was found after taking into account dead or noisy channels. The hit efficiency was estimated by measuring the number of good tracks with a hit close to the extrapolated intersection of a given sensor that was excluded from the track fit itself. Tracks which intersect regions with known bad channels or very close to in the edge region are excluded in the calculation of the single hit efficiency. The hit efficiency, see Fig. 16, was measured to be above 98% and fairly uniform across the SVT. The spatial resolution of similar microstrip sensors is well established by test beam data, against which the charge deposi-

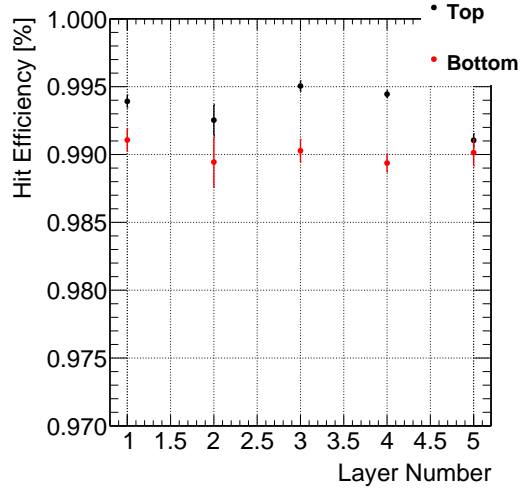


Figure 16: The hit reconstruction efficiency as a function of detector layer.

tion model in the simulation is validated. This resolution can be parameterized as a function of the total signal to single-strip noise (S/N) and the crossing angle of tracks through the sensor. The single-hit resolution for charged particles with signal to noise ratio above 20, as demonstrated here, is relatively constant at approximately  $6 \mu\text{m}$  for tracks that enter approximately normal to the sensors as in HPS.

### 7.1.2. Momentum and Vertexing Resolution

By selecting  $e^+e^-$  pairs from the triggered events we are able to study basic distributions of pair production kinematics and in particular those related to our vertex performance. Pairs of opposite charge tracks, one in the top and one in the bottom half of the SVT, with momentum larger than 400 MeV were selected. The pair production kinematics are relatively well reproduced given the alignment of the tracker; Fig. 17 shows the invariant mass and ratio of electron momentum over the sum of electron and positron.

We estimate the accuracy of the SVT momentum scale and resolution by looking at the agreement between data and simulation in the shape of the kinematic distributions for single- and two track events. By adjusting the overall momentum scale and smearing the simulated events with a Gaussian resolution we estimate an uncertainty of 10% on both the momentum scale and resolution in the Test run. The expected momentum resolution from simulation is between 4-5% for tracks in the momentum range of the Test run.

For the vertexing performance the foremost difference compared to electron beam running is that the target was located approximately 67 cm from our nominal target position; giving almost collinear tracks in the detector. This degrades the vertex resolution along the beam line compared to that expected in an electron beam with tracks from the nominal target position. Furthermore, tails of the vertex distributions are impossible to study with the finite data sample obtained in the Test run. Nevertheless, useful information can still be obtained by studying the vertex distributions. Figure 18 shows the distance of closest approach of the momentum vectors extrapolated in the upstream direction from our analyzing magnet, taking into account the measured fringe field of the PS magnet.

### 7.2. ECal Performance

The integrated pulse of each channel was converted to energy by first subtracting the pedestal and

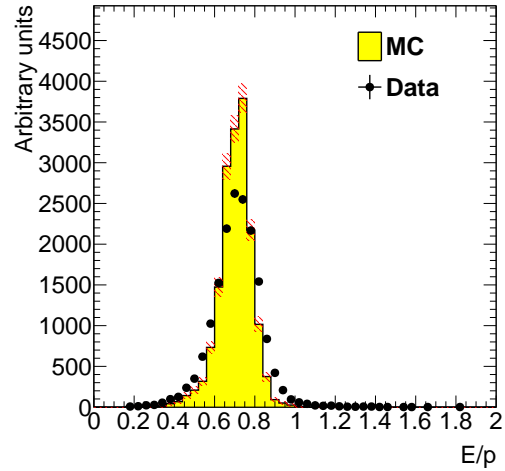


Figure 19: The ECal energy over track momentum ratio comparing data and simulation

then applying a conversion factor to convert ADC counts to energy. The pedestals are measured using special runs where each trigger records 100 samples of signals from the APDs with 4 ns between each sample. The pedestals were extracted from the part of the window before the actual hit in the calorimeter. After subtracting the pedestal, modules with integrated pulse above a threshold are clustered using a simple algorithm similar to the one deployed for the trigger (see Sec. 6.1). Due to the high effective readout threshold of 73 MeV the average number of modules in a cluster was  $\sim 3$  and the simple clustering algorithm worked well for reconstruction of the detected shower energy. An average noise level of approximately 15 MeV was measured in special pedestal runs.

The ratio of the ECal cluster energy  $E$  to the momentum  $p$  of a matched track in the SVT was used to determine the conversion factors from ADC counts to energy. To compare data and simulation, all inoperable or noisy channels in the SVT and ECal was disabled in both data and simulation; any efficiency or bias that affect the data should be reflected in the simulation. representing the average  $E/p$  for clusters that include the crystal Iteratively, conversion coefficients for each module is adjusted until the  $E/p$  ratio in data and simulation are similar. The distribution of the  $E/p$  ratio in data and simulation can be seen in Fig. 19. The peak position of the distribution indicates the sampling fraction of the ECal, the fraction of the incident particle energy measured in the cluster. The width and tails of the distribution in data indicates imperfect calibration and noise

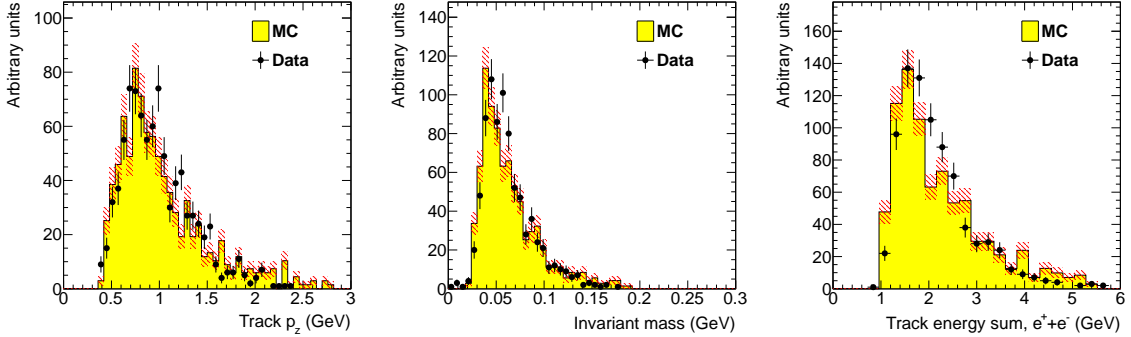


Figure 17: Kinematic distributions for  $e^+e^-$  pairs selected by opposite charged tracks in the top and bottom half of the tracker: track momentum in the top half of the SVT (left), invariant mass (middle) and the sum of the track momentum for the pair (right).

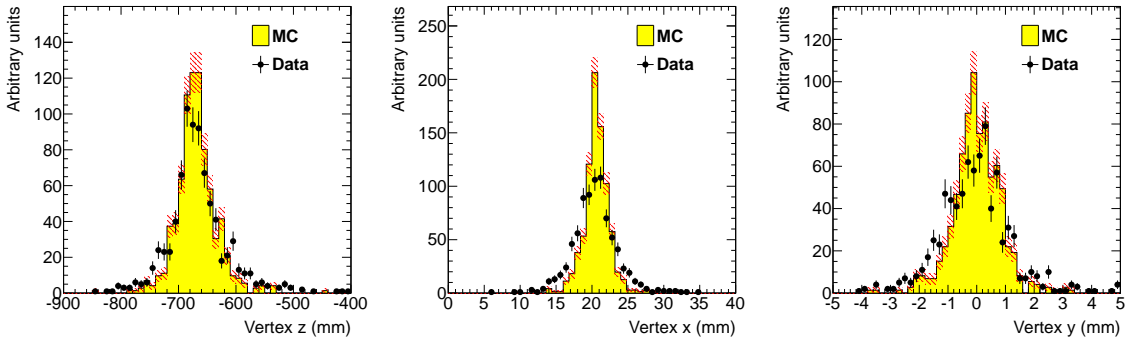


Figure 18: Vertex position represented by the distance of closest approach of the extrapolated momentum vectors upstream of the PS magnet taking into account the measured fringe field. The overall shift from zero in the x-direction is due to a 30 mrad rotation of the SVT with respect to the beam line.

of the ECal modules. This level of calibration and the agreement with simulation was found to be sufficient for the multiple scattering analysis using normalized event rates described in Sec. 8.

### 7.3. Trigger Performance

The trigger and DAQ integrate pulses from the ECal modules differently to measure the energy deposited in the each crystal. The trigger integrates the pulse using a time-over-threshold window, and the DAQ readout integrates using a fixed-size window (5 samples before and 30 samples after a threshold crossing). For every event, the trigger reports the trigger decision as a bit mask (top half, bottom half or both) and the time the trigger fired. The trigger performance was studied by simulating the trigger for each event and comparing to how the events were actually triggered. First, we simulate the FADC readout board to convert from readout hits (with fixed-size window integration) to trigger hits (time-over-threshold integration). Secondly, the CTP

clustering algorithm and the trigger decision is simulated before we compare the trigger decision and trigger time to what was reported by the actual trigger. To eliminate trigger bias, we use a tag and probe method. To study the trigger performance in one half of the ECal, we select events which triggered the other half and where there was exactly one probe cluster in the ECal half under study. We then measure trigger efficiency as the fraction of tagged events that fired the trigger in the probe half as a function of the probe cluster energy, shown in Fig. 20. As a cross-check, the turn-on from the trigger threshold was measured to be 1280 in units of ADC counts as expected. The threshold was not perfectly sharp because of uncertainties in the conversion from readout to trigger hits described above, but based on comparisons with simulation we found that the trigger worked exactly as specified. The trigger turn-on is slow and reaches an uneven plateau just below 1 GeV for two reasons; gain variations between different crystals lead to the threshold variations and the nonlinearity

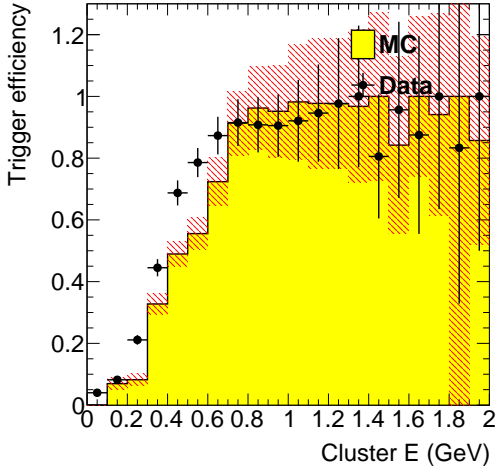


Figure 20: Trigger efficiency in both halves of the ECal for data and simulation as a function of cluster energy.

of the time-over-threshold integral means that the effective threshold is higher for clusters that span multiple crystals. The effective trigger threshold is therefore dependent on position and energy of the particle as well as cluster multiplicity.

## 8. Multiple Coulomb Scattering Distributions

Occupancies close to the beam create many of the key challenges in the HPS experiment and determine the limits of sensitivity to low  $A'$  masses. These occupancies are dominated by electrons which have multiple Coulomb scattered (MCS) to relatively large angles in the target. Because HPS is sensitive to scattering angles far out on the tail of the MCS distribution, well beyond the angles important in other experiments, care must be taken to ensure our simulations are correct in this regime.

### 8.1. Multiple Coulomb Scattering Models

One of the main goals of the HPS Test was to evaluate the description of the tails of the MCS to gain further confidence in the expected detector occupancy in the full HPS experiment. Previous studies of multiple scattering angles show good agreement with the Molière theory [18] for a wide range of materials and projectiles [19, 20, 21]. We have verified that the angular distribution  $F(\theta)$  in the differential cross section  $d\sigma = F(\theta)d(\cos \theta)d\phi$  for the EGS5 [22] simulation program show good agreement with Molière's analytical

formula as formulated by Bethe [23]. The small angle approximation was also shown to be in agreement with the theory formulated by Gaudsmitt and Saunderson [24, 25] that is valid for any angle. While EGS5 uses the more complex and time consuming Molière formula, the default physics list of GEANT4 uses the so-called Urban model, an approximation with two, continuously joined, functions to take into account small and large angle scattering. Due to the explicit function in large angle approximation used by GEANT4 we expect that GEANT4 will overestimate the angular distribution at angles larger than a few mrad.

Figure 21 gives a schematic view of the main differences between the photon and electron beam setup. The

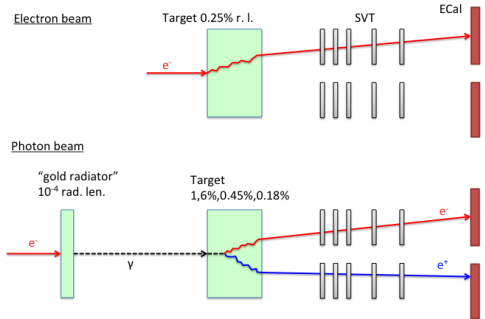


Figure 21: Schematic comparison of HPS Test run photon beam compared to the HPS electron beam.

angular distribution of the pair produced electron and positron emerging from the converter in the test run has comparable contributions from *i*) the pair production angle and *ii*) the MCS of the electron and positron in the converter after production. By measuring the scattering rate at several different converter thicknesses we can vary the contribution from MCS while the contribution from the pair production angle is constant. This allows us to confirm our model of MCS despite the fact that all data was taken with a photon beam.

### 8.2. Running Conditions

Data was taken at three different converter thicknesses with a beam current varying between 30 – 70 nA, see Tab. 3. The photon beam line during the test run produced a relatively large fraction of pairs originating upstream of the converter. This contribution was measured during data taking with “empty” converter runs i.e. removing the converter but with all other conditions the same. The upstream background measured

Converter thickness (% $X_0$ )	Duration (s)	$e^-$ on converter ( $\mu\text{C}$ )
1.6	911	24.4
0.18	2640	193.5
0.45	2149	140.7
0	1279	88.1

Table 3: Measured integrated currents for the dedicated photon runs.

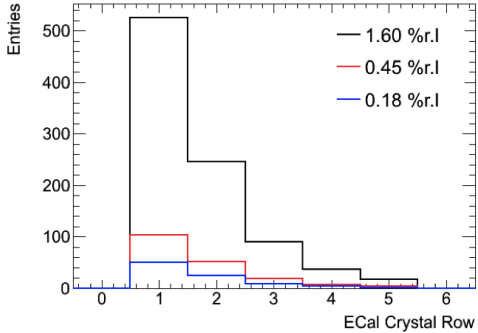


Figure 22: Measured vertical angular distributions after integrated beam current normalization and background subtraction.

in the “empty” converter runs was subtracted from the other runs, properly normalized using the measured integrated currents.

### 8.3. Measured Angular Distributions

For this analysis, we measure angular distribution of electrons and positrons using the ECal. Cluster reconstruction was done using the algorithm described in Sec. 6.1 build clusters around seed hits (hits above a “seed” energy threshold and with greater energy than any neighboring hits), and add all neighboring hits above an “add” energy threshold. Hit energy is calibrated by matching track momentum to cluster energy, as described in Sec. 7.2. The measured angular distribution in the ECal for the three converter thicknesses are shown in Fig. 22. The data has been normalized to the integrated beam current and the background has been subtracted. The background fraction for the three converter thicknesses was 16%, 52% and 71% for converter thicknesses of 1.6%, 0.45% and 0.18%, respectively. The background fraction was also cross-checked by pointing back tracks reconstructed in the SVT to identify the fraction of tracks not emanating from the converter. We also checked that the contribution from photons to our triggered sample was less than 2% (without angular selections which would further reduce the

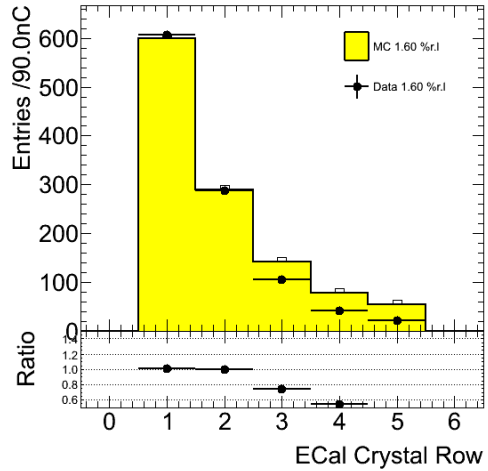


Figure 23: Comparison between the observed and predicted angular distribution using EGS5 for a converter thickness of 1.6%. Similar agreement is found for 0.45% and 0.18% converter thicknesses. Only statistical uncertainties are shown.

Converter (% r.l.)	1.60	0.45	0.18
EGS5	$1162 \pm 112$	$255 \pm 28$	$94 \pm 17$
GEANT4	$2633 \pm 250$	$371 \pm 38$	$114 \pm 18$
Observed	$1064 \pm 2$	$196 \pm 1$	$92 \pm 1$

Table 4: Observed and predicted number of events for 1 s of beam at 90 nA for three different converter thicknesses. The uncertainty on the prediction includes systematic uncertainties.

contribution).

These measured angular distributions are compared to simulation to validate the modeling of the MCS. EGS5 [22] is used to generate the electromagnetic interactions in the converter while GEANT4 is used to simulate the particles after the converter. Figure 23 shows the angular distribution comparing data and EGS5 normalized to 1 s of beam at 90 nA beam current with a converter thickness of 1.6%. Reasonable agreement is obtained in the most important region close to the beam. There is a hint of a slightly different slope of the data at larger angles; this difference is covered by systematic uncertainties. The total rates for each converter thickness is shown in Fig. 24 and summarized in Tab. 8.3.

The total systematic uncertainty was estimated to be between 10–18% depending on the run including: a 5% uncertainty on the integrated current normalization, alignment of the ECal, uncertainty from the background normalization, and limited Monte Carlo statistics.

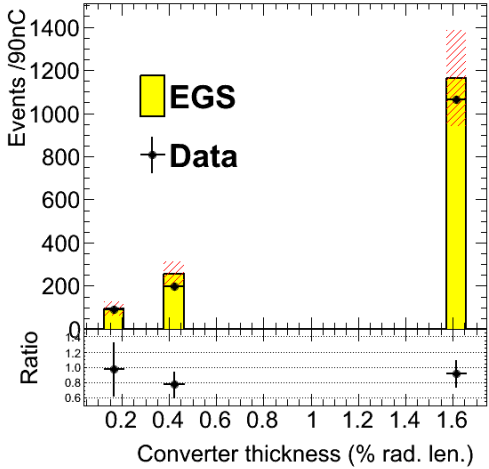


Figure 24: The measured rate as a function of converter thickness for data and EGS5 simulation of MCS in the converter.

#### 8.4. Conclusion

In summary, the accurate modeling of the MCS is fundamental to estimate occupancies and trigger rates for HPS. EGS5 predicts the correct angular distribution across all converter thicknesses as expected while GEANT4, using the so-called Urban model for multiple scattering overestimates the rates; with the disagreement increasing with larger converter thickness. This preliminary result verifies similar studies [1] and gives confidence in our modeling of the MCS using EGS5 for evaluating the physics reach of HPS.

### 9. Summary and Outlook

The HPS Test Run experiment, using a simplified version of the apparatus planned for the full HPS experiment in a parasitic photon beam, demonstrated the feasibility of the detector technologies proposed for the HPS silicon tracker, ECal, and data acquisition systems. Performance from each of these subsystems has been shown to be adequate to conduct the full experiment successfully. A measurement of the normalized trigger rates from a photon conversion target confirmed expectations from simulation, giving credence to estimates of the trigger rates and the detector backgrounds expected in electron beam running.

### 10. Acknowledgements

### References

- [1] O. Adriani, et al. (PAMELA Collaboration), An anomalous positron abundance in cosmic rays with energies 1.5-100 GeV, *Nature* 458 (2009) 607–609.
- [2] M. Ackermann, et al. (Fermi LAT Collaboration), Measurement of separate cosmic-ray electron and positron spectra with the Fermi Large Area Telescope, *Phys.Rev.Lett.* 108 (2012) 011103.
- [3] B. Holdom, Two U(1)'s and Epsilon Charge Shifts, *Phys.Lett.* B166 (1986) 196.
- [4] N. Arkani-Hamed, D. P. Finkbeiner, T. R. Slatyer, N. Weiner, A Theory of Dark Matter, *Phys.Rev.* D79 (2009) 015014.
- [5] J. D. Bjorken, R. Essig, P. Schuster, N. Toro, New Fixed-Target Experiments to Search for Dark Gauge Forces, *Phys.Rev.* D80 (2009) 075018.
- [6] A. G. et al. (HPS Collaboration), HPS Heavy Photon Search Proposal, 2010.
- [7] A. G. et al. (HPS Collaboration), HPS Test Run Proposal to DOE, 2011.
- [8] I. Rashevskaya, S. Bettarini, G. Rizzo, L. Bosisio, S. Dittongo, et al., Radiation damage of silicon structures with electrons of 900-MeV, *Nucl.Instrum.Meth.* A485 (2002) 126–132.
- [9] S. A. et al., Geant4a simulation toolkit, *Nucl.Instrum.Meth.* A506 (2003) 250 – 303.
- [10] N. A. Graf, org.lcsm: Event reconstruction in Java, *J.Phys.Conf.Ser.* 331 (2011) 032012.
- [11] D. S. Denisov, S. Soldner-Rembold, D0 Run IIB Silicon Detector Upgrade: Technical Design Report (2001).
- [12] M. French, L. Jones, Q. Morrissey, A. Neviani, R. Turchetta, et al., Design and results from the APV25, a deep sub-micron CMOS front-end chip for the CMS tracker, *Nucl.Instrum.Meth.* A466 (2001) 359–365.
- [13] M. Friedl, C. Irmler, M. Pernicka, Readout of silicon strip detectors with position and timing information, *Nucl.Instrum.Meth.* A598 (2009) 82–83.
- [14] R. Larsen, Emerging New Electronics Standards for Physics, *Conf.Proc.* C110904 (2011) 1981–1985.
- [15] A. Radyushkin, P. Stoler (Eds.), Inner Calorimeter in Clas/dvcs Experiment, 2008.
- [16] D. H., et al., Integrated tests of a high speed VXS switch card and 250 MSPS flash ADCs, 2007. doi:10.1109/NSSMIC.2007.4436457.
- [17] L. Jones, APV25-S1: User guide version 2.2, RAL Microelectronics Design Group, 2011.
- [18] G. Moliere, Theory of the scattering of fast charged particles. 2. Repeated and multiple scattering, *Z.Naturforsch.* A3 (1948) 78–97.
- [19] D. Attwood, P. Bell, S. Bull, T. McMahon, J. Wilson, et al., The scattering of muons in low Z materials, *Nucl.Instrum.Meth.* B251 (2006) 41–55.
- [20] G. Shen, C. Ankenbrandt, M. Atac, R. M. Brown, S. Ecklund, et al., Measurement of Multiple Scattering at 50-GeV/c to 200-GeV/c, *Phys.Rev.* D20 (1979) 1584.
- [21] B. Gottschalk, A. Koehler, R. Schneider, J. Sisterson, M. Wagner, Multiple coulomb scattering of 160 mev protons, *Nuclear Instruments and Methods in Physics Research Section B: Beam Interactions with Materials and Atoms* 74 (1993) 467 – 490.
- [22] H. Hirayama, Y. Namito, A. Bielajew, S. Wilderman, W. Nelson, The EGS5 Code System, 2005.
- [23] H. Bethe, Moliere's theory of multiple scattering, *Phys.Rev.* 89 (1953) 1256–1266.

- [24] S. Goudsmit, J. Saunderson, Multiple Scattering of Electrons, Phys.Rev. 57 (1940) 24–29.
- [25] S. Goudsmit, J. Saunderson, Multiple Scattering of Electrons. II, Phys.Rev. 58 (1940) 36–42.